



HAL
open science

Intertrack surface losses in miniature coplanar waveguide on silicon-on-insulator

Jaouad Marzouk, Vanessa Avramovic, S. Arscott

► **To cite this version:**

Jaouad Marzouk, Vanessa Avramovic, S. Arscott. Intertrack surface losses in miniature coplanar waveguide on silicon-on-insulator. *Journal of Physics D: Applied Physics*, 2021, 54 (4), pp.045102. 10.1088/1361-6463/abbc36 . hal-03094146

HAL Id: hal-03094146

<https://hal.science/hal-03094146v1>

Submitted on 6 Jan 2021

HAL is a multi-disciplinary open access archive for the deposit and dissemination of scientific research documents, whether they are published or not. The documents may come from teaching and research institutions in France or abroad, or from public or private research centers.

L'archive ouverte pluridisciplinaire **HAL**, est destinée au dépôt et à la diffusion de documents scientifiques de niveau recherche, publiés ou non, émanant des établissements d'enseignement et de recherche français ou étrangers, des laboratoires publics ou privés.

Intertrack surface losses in miniature coplanar waveguide on silicon-on-insulator

Jaouad Marzouk, Vanessa Avramovic and Steve Arscott^{a)}

Institut d'Electronique, de Microélectronique et de Nanotechnologie (IEMN), CNRS UMR8520, The University of Lille, Cité Scientifique, Avenue Poincaré, 59652 Villeneuve d'Ascq, France.

^{a)}E-mail: steve.arscott@univ-lille.fr

Abstract

Attenuation has been studied in different-sized coplanar waveguide (CPW) patterned onto silicon-on-insulator (SOI) for three different surfaces between the CPW tracks: silicon dioxide/silicon interface, a hydrogen-terminated silicon surface, and a native oxide. For large-gap CPW (signal track width $s = 100 \mu\text{m}$, gap width $g = 63.5 \mu\text{m}$), selective removal of the silicon dioxide from between the metal tracks reduces losses from 0.79 dB mm^{-1} to 0.69 dB mm^{-1} at 50 GHz. The subsequent growth of a native oxide on the silicon surface between the tracks results in losses equal to 0.67 dB mm^{-1} . For small-gap CPW ($s = 2 \mu\text{m}$, $g = 2.5 \mu\text{m}$), losses are reduced from 5.6 dB mm^{-1} to 3.4 dB mm^{-1} at 50 GHz by selectively removing the silicon oxide between the metal tracks. However, when a native oxide is allowed to grow on the silicon surface between the tracks, the losses increase significantly to 5.8 dB mm^{-1} . When the native oxide is removed, the losses decrease to those observed following removal of the silicon dioxide. The measurements suggest that the contribution of the intertrack surface losses is the result of free-carrier losses due to a surface inversion layer. The surface-associated losses are proportionally larger as the CPW dimensions shrink—as predicted by modelling. We suggest that technologies employing miniature CPW should take this into account. The native oxide should be routinely removed if possible—implying that

appropriate chemically-resistant metallisation be chosen, or fabrication processes should incorporate stable passivation of silicon surfaces between CPW tracks to avoid native oxide growth. Conversely, the increased sensitivity of attenuation to surface effects by shrinking CPW dimensions suggests that CPW-based sensors could benefit from miniaturization.

Keywords: miniature coplanar waveguide, intertrack surface losses, silicon dioxide, hydrogen-terminated silicon, native oxide, silicon-on-insulator, free-carrier losses

1. Introduction

Coplanar waveguides (CPW) [1,2] have long been a key component in radio frequency (RF) circuits and integrated circuits (IC) [3]. CPW are also important elements in emerging technologies such as quantum computing [4] and associated circuitry [5], miniature microelectromechanical systems (MEMS) based probe technologies [6], non-invasive biosensors [7], and for high frequency characterization of a variety of materials [8–12]. An understanding of signal attenuation (due to losses) in CPW is therefore critical for both RF circuits [13,14] and for emerging applications [15,16], which can involve miniature CPW [16–18] to enhance performance—where characterization and understanding of losses are relatively less-well documented. Losses in CPW depend on both materials and architecture [2], and more recently the impact of microfabrication on losses has been astutely pointed out [19–22]. In practical quantum computing, it has been proposed that performances can be enhanced by *increasing* circuitry gap size—since a smaller proportion of the electric field interacts with potentially-lossy interfaces, e.g. substrate-air interfaces [23]—although this approach would seem to be at cross purposes with the ethos of Moore’s law in microelectronics. In this context, both silicon [24] and silicon-on-insulator (SOI) [25] are technologically important for a wide range of applications. The primary loss mechanisms which cause signal attenuation in CPW patterned onto silicon or SOI are relatively well understood. These are conductor losses in tracks and dielectric losses in the bulk silicon. Less well understood are interface losses associated with buried interfaces (e.g. buried silicon dioxide/silicon interfaces under and between the CPW tracks) and intertrack surface losses (e.g. the surface of the silicon between the conducting tracks). Here we study the effect of CPW size and intertrack surface type (silicon dioxide, hydrogen-terminated silicon, and a native silicon oxide) on intertrack surface losses associated with the silicon surface between conducting tracks.

2. Coplanar waveguide design and fabrication

2.1. Coplanar waveguide design

Two types of CPW were designed for the study, which we refer to as: ‘large-gap’ CPW and ‘small-gap’ CPW—the principal dimensions of which are given in Table 1. The design of the CPW was performed using commercial software (Comsol Multiphysics®, USA). As the small-gap CPW are too small to be directly probed by commercial microwave probes (Cascade Microtech, USA), their CPW design incorporated transition elements from the small-gap CPW to large-gap CPW—the latter terminating in large contact pads compatible with commercial probe dimensions. The design of the CPW aimed at an impedance of 50 ohms in the measured frequency range i.e. minimal signal reflection between the different parts of the CPW ensembles.

Table 1. Dimensions of the large-gap and small-gap CPW. The metallization (Cr/Au) thickness is 10/500 nm.

CPW type	Signal S width w (μm)	G-G distance (μm)	S-G gap g (μm)	Length L (μm)
Large-gap	100	227	63.5	1400
Small-gap - type 1	2	7	2.5	200
Small-gap - type 2	2	7	2.5	400
Small-gap - type 3	2	7	2.5	800

2.2. Fabrication of the coplanar waveguides

Wafer-bonded SOI [26] wafers were purchased for the study (Si-Mat, Germany). The SOI wafers have the following specifications which are relevant to the current study: the silicon device layer is 20 ± 0.5 μm thick, (electrical resistivity $\rho > 1000$ Ω cm – p-type background doping $< 1.47 \times 10^{13}$ cm^{-3}) and a (100) orientation. The buried silicon dioxide layer, commonly known as the ‘BOX’, is 2 ± 0.1 μm thick. The

silicon ‘handle’ is 400 ± 20 μm thick, resistivity >1000 $\Omega\text{ cm}$ – also p-type background doping, and a (100) orientation.

A set of lithographic masks was designed for the microfabrication process using Layout Editor software (Juspertor GmbH, Germany)—the principle microfabrication steps can be found in the Supplementary Information. The microfabrication of the CPW was performed in a class ISO 5/7 cleanroom ($T = 20\pm 0.5^\circ\text{C}$; $RH = 45\pm 2\%$). Prior to processing, the SOI wafers are cleaned [27]. A 50 nm thick silicon dioxide layer was deposited onto the surface of the SOI wafer using low pressure chemical vapor (LPCVD) techniques (silane SiH_4 /oxygen O_2 — 850°C). The silicon dioxide was annealed in N_2 at a temperature of 1000°C for 60 minutes. Following this, the metallic CPW tracks were deposited onto the surface of the wafers using evaporated chromium/gold (thickness: 10/500 nm) bilayer patterned via electron beam (ebeam) lithography and *lift-off* techniques [6]. A Cr/Au metallization was used as it is relatively chemically resistant to aqueous solutions of hydrofluoric (HF) acid [28]—the wafers were to be treated with a ‘buffered’ HF solution later in the study. In a separate step, large area contact pads were also metallised (total pad thickness of Cr/Au: 10/1000 nm) onto the ends of the CPW to facilitate the microwave probing. Finally, the 400 μm thick silicon handle wafer was etched away from parts of the wafer to form a 20 μm thick silicon membrane which supports the small-gap CPW. This was achieved using front-to-back photolithography and deep silicon etching [6].

Figure 1 shows optical microscopy images taken of the small-gap CPW using a VHX-6000 numerical digital microscope (Keyence, France).

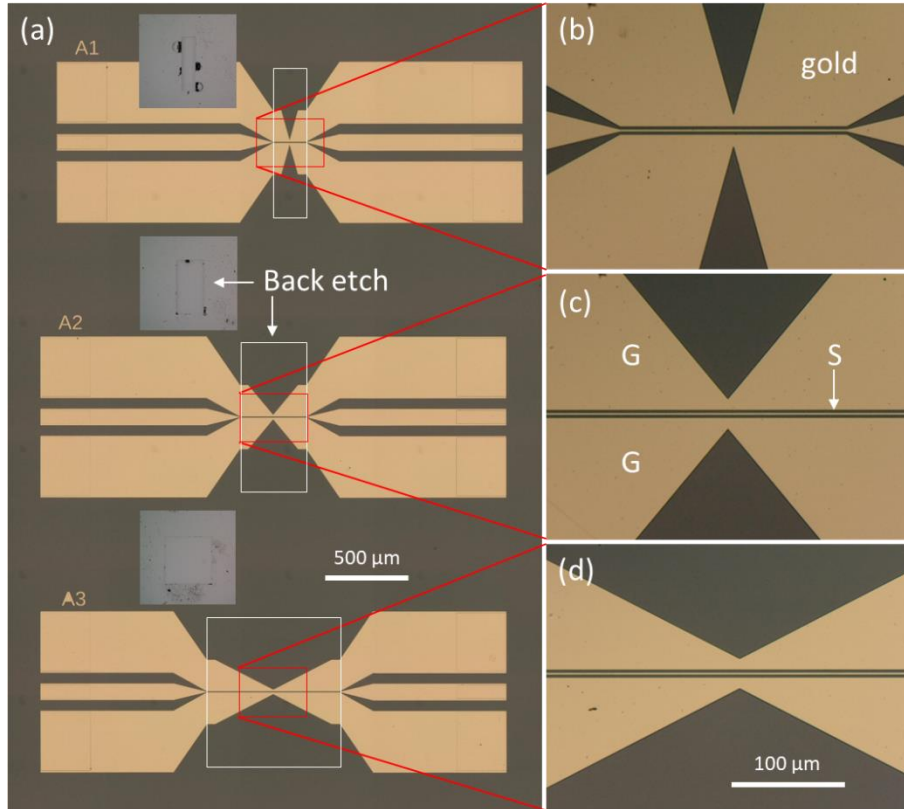


Figure 1. Optical microscopy images of the small-gap coplanar waveguides (CPW) systems fabricated for the study. (a) Three types of small-gap CPW: having length equal to 200 μm (A1), 400 μm (A2), and 800 μm (A3). Zoom images of the small-gap CPW central conductor of width 2 μm for A1 (b), A2 (c), and A3 (d). The patterned Cr/Au thickness of the CPW is 10/500 nm—the contact pad thickness is 10/1000 nm. Parts of the 400 μm thick silicon handle wafer have been removed using rear-face deep etching—this is indicated on the front-face photographs by the white quadrilaterals which correspond to the suspended section of the CPW. The small insets (grey) are photographs of the rear side of the SOI wafer indicating these deep etches—they are 200 $\mu\text{m} \times 800 \mu\text{m}$, 400 $\mu\text{m} \times 800 \mu\text{m}$, and 800 $\mu\text{m} \times 800 \mu\text{m}$.

The small-gap CPW systems contained sections of suspended, small-gap CPW of varying length (200 μm , 400 μm , and 800 μm), plus a ‘small-gap to large-gap’ transition region, larger CPW, and contact pads. The chips also contained large-gap CPW (not shown). In the case of the small-gap CPW, parts of the

400 μm thick silicon handle wafer have been removed from directly under the small-gap sections using rear-face deep etching—this is indicated in Fig. 1(a) by the white square. The small insets (grey) are photographs of the rear side of the SOI wafer indicating the deep etch. In Fig. 1, the 50 nm thick silicon dioxide layer is still present between the Cr/Au metal tracks. The surface roughness and thickness of the evaporated Cr/Au layer was measured to increase accuracy of the modelling of the conductor losses. Atomic force microscopy (AFM) measurements revealed an average roughness (Ra) of the gold surface equal to 3.6 ± 0.2 nm. The thickness of the evaporated metal tracks was measured to be 510 ± 5 nm using a DektakXT surface profiler (Bruker, USA).

3. Methods and materials

3.1. Description of the chip surfaces for the microwave characterization

Figure 2 shows cross-sectional schematic diagrams describing the four CPW intertrack surfaces used for the microwave characterization. The CPW (large-gap and small-gap) were first characterized directly after device processing. In this configuration, the 50 nm-thick silicon dioxide layer is present between the signal and ground tracks of the CPW—see Fig. 2(a). Following this, the silicon dioxide layer was selectively-etched away from between the CPW gaps using a VLSI grade ‘buffered HF’ solution composed of a 7:1 volume mixture of NH_4F (40 wt %) and HF (49 wt%). For this etch solution, the annealed silicon dioxide etch rate is approximately 150 nm min^{-1} [29]. Note that the 1 μm thick buried oxide layer—which is present underneath the 20 μm thick silicon membranes—is only partially etched away during this wet etch step—see Supplementary Information. Note also that the Cr/Au tracks are not etched by this solution [28]. The chips were inspected using a microscope at this point to ensure no damage was incurred to the CPW tracks—especially in the case of the small-gap CPW—see Supplementary Information.

The hydrogen-terminated silicon [30] surface between the CPW tracks is shown in Fig. 2(b) and indicated schematically by: —H. The freshly-etched CPW samples were directly transported to a clean characterization environment (ISO 8 environment: $T = 20 \pm 2^\circ\text{C}$ $RH = 50 \pm 10\%$) in a closed box. Microwave measurements were immediately performed (in air) on the CPW (<1 hour after etching of the SiO_2 layer).

Following these measurements, the samples were stored in the ISO 8 characterization environment in a closed sample box and measured after a further 3 months and 5 years—see Fig. 2(c). Despite the stability of the hydrogen-terminated (100) silicon surface following exposure to HF-based solutions [31]; if exposed to oxygen, the surface will slowly begin to oxidize with time [32]. Exposure of a silicon surface to air at room temperature results in the formation of what is commonly referred to as a ‘native silicon oxide’ on the surface of the silicon between the metal tracks. This is shown in Fig. 2(c), where the native oxide is schematically indicated by: —O. To avoid confusion, what is referred to here as a ‘native oxide’ is an oxidized silicon surface resulting from an initially hydrogen-terminated silicon surface exposed to air at room temperature for a long period of time. Finally, after 5 years of native oxide growth, the native oxide was selectively removed from the silicon surface between the CPW metal lines using buffered HF (10 seconds) to leave a hydrogen-terminated silicon surface between the CPW metal tracks—this measurement configuration is shown in Fig. 2(d).

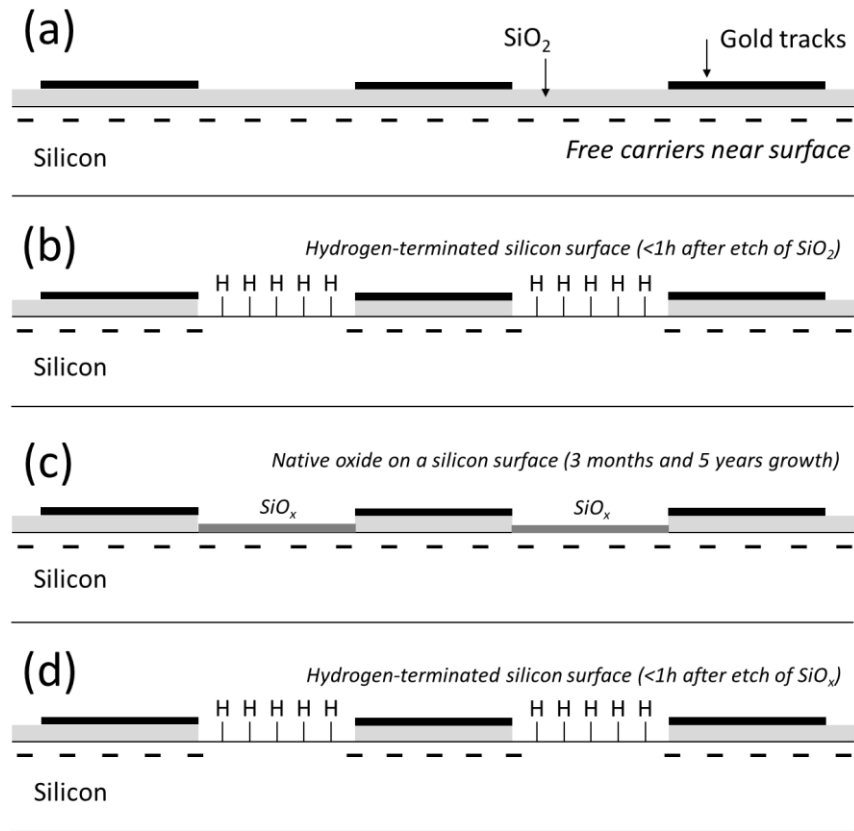


Figure 2. The four main intertrack surface configurations used for the microwave characterization of the CPW. (a) CPW with a 50 nm thick SiO_2 layer present between the CPW tracks, (b) CPW with a hydrogen-terminated (schematically represented by: —H) silicon surface between the CPW tracks following removal of the SiO_2 using a buffered HF-based solution (measurement performed <1 hour after etching), (c) CPW following subsequent growth of the native oxide (SiO_x) on the silicon surfaces between the CPW tracks (measurement performed after 3 months and 5 years of exposure to air at room temperature), and (d) CPW with a hydrogen-terminated silicon surface between the CPW tracks following removal of the SiO_x native oxide using a buffered HF-based solution (measurement performed <1 hour after etching). The presence of excess free carriers near interfaces or surfaces (compared to the bulk) is represented by a (-).

The current study was designed to isolate and quantify the interface losses in each case—allowing the contribution of the intertrack surface losses to be determined. The measurements were performed on the same wafers prior to, and following, chemical treatments. In this way, it is reasonable to assume—at least in a first approximation—that the conductor, substrate losses, and interface losses (both underneath the tracks and at buried interfaces) are independent of intertrack surface modifications. The presence of the charges (-) in Fig. 2 will be discussed in Section 6.

3.2. Microwave characterization methods

The microwave measurements were conducted using a N5245A vector network analyser (VNA) (Agilent Technologies, USA) and commercial ground-signal-ground RF probes (Cascade Microtech, USA). **A standard line-reflect-reflect-match (LRRM) calibration [33] of the VNA plus the RF probes using a commercial impedance standard substrate was performed before the measurements.** This is an important point to be able to accurately extract the insertion loss as a function of frequency, CPW size, and intertrack surface configuration from the measurements.

The microwave characterization measures the scattering ‘S’ parameters. Assuming the two ports have the same reference impedance, the insertion loss (*IL*)—given in decibels (dB)—is calculated from the absolute value of the forward transmission coefficient S_{21} using the following equation [34]:

$$IL = -20 \log_{10} |S_{21}| \quad (1)$$

where S_{21} for a two-port network is given by:

$$S_{21} = \frac{b_2}{a_1} \quad (2)$$

where a_1 is the incident travelling voltage wave at port 1 and b_2 is the exiting travelling voltage wave at port 2. Therefore $|a_1|^2$ and $|b_2|^2$ correspond to the values of the incident and exiting powers. The

attenuation coefficient α_{dB} (dB per unit length) of the transmission line can be obtained by dividing the measured (or extracted—as in the case of the small-gap CPW here) insertion loss by the length of the CPW.

The input source power and the intermediate frequency bandwidth are set respectively to -10 dBm (0.1 mW) and 100 Hz. As $z_i \sim z_L \sim z_o = 50 \Omega$ then $S_{21} \gg S_{11}$ and S_{22} . The experimental results presented in the following are based on averages from several measurements conducted on the same lines and on equivalent lines found on the SOI wafer.

4. Experimental results

4.1. Microwave characterization of large-gap coplanar waveguides

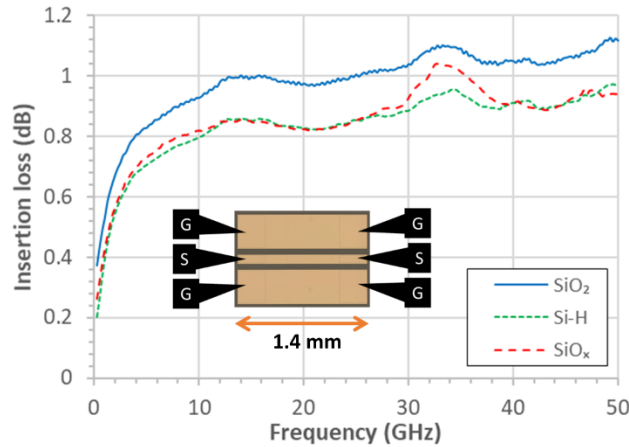


Figure 3. Measured insertion losses of the large-gap CPW as a function of applied frequency for 3 CPW intertrack surface configurations: with a silicon dioxide layer between the metal tracks (solid blue line— SiO_2), a hydrogen-terminated silicon surface between the metal tracks (short-dashed green line— Si-H), and with a native oxide on the silicon surface between the metal tracks (long-dashed red line— SiO_x). The CPW have a length L of 1.4 mm, a signal line width s equal to $100 \mu\text{m}$, and a signal-to-ground gap width g equal to $63.5 \mu\text{m}$.

Figure 3 shows the measured insertion loss (given in dB) of the large-gap CPW as a function of applied measurement frequency (from 0.25 GHz to 50 GHz) for three different CPW intertrack surface configurations. First, measurements taken with a 50 nm thick silicon dioxide present between the CPW tracks (solid blue line—SiO₂). Second, measurements taken 1 hour after the silicon dioxide has been selectively-etch away from between the CPW tracks using the buffered HF solution (short-dashed green line—Si-H)—this results in a hydrogen-terminated silicon surface. And thirdly, after 3 months of native oxide growth on the hydrogen-terminated (100) silicon surfaces between the CPW tracks in air at room temperature (long-dashed red line—SiO_x). The inset to Fig. 3 shows a plan view of a large-gap CPW being probed. The curves presented in Fig. 3 are averages based on several measurements from different CPW of this type found on the SOI wafer, the mean standard deviations of the measurements are: ±0.05 dB (SiO₂), ±0.02 dB (Si-H), and ±0.04 (SiO_x). The peaks in the curves can be attributed to non-ideal calibration [35]. The return losses (S_{11} and S_{22}) are less than -24 dB for these measurements—plots of these data can be found in the Supplementary Information.

4.2. Microwave characterization of small-gap coplanar waveguides

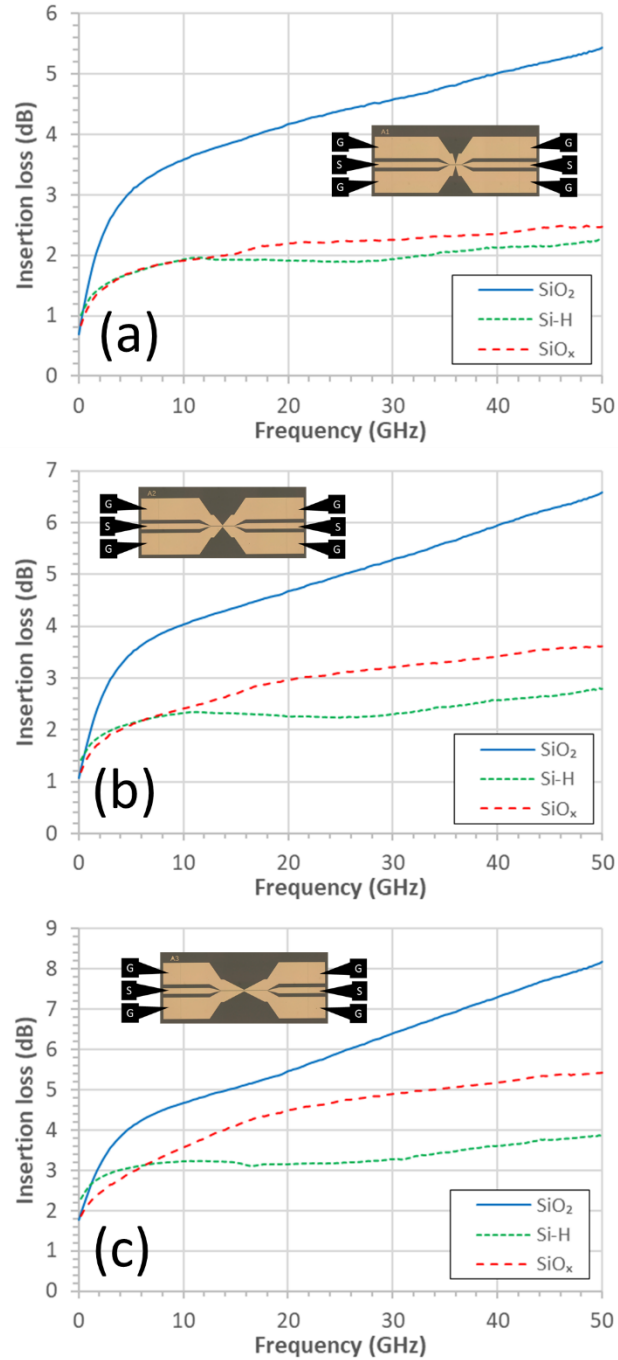


Figure 4. Measured insertion losses of the small-gap CPW systems as a function of applied frequency. The CPW have a length L equal to: (a) $200 \mu\text{m}$, (b) $400 \mu\text{m}$, and (c) $800 \mu\text{m}$. All small-gap CPW have a signal line width s equal to $2 \mu\text{m}$, and a signal-to-ground gap width g equal to $2.5 \mu\text{m}$. The CPW intertrack surface configurations are: with a silicon dioxide layer between the metal tracks (solid blue

line—SiO₂), a hydrogen-terminated silicon surface between the metal tracks (short-dashed green line—Si-H), and with a native oxide on the silicon surface between the metal tracks (long-dashed red line—SiO_x).

Figure 4 shows the measured insertion loss (given in dB) of small-gap CPW systems—incorporating sections of different small-gap CPW lengths (200 μm, 400 μm, and 800 μm)—as a function of applied measurement frequency (GHz) for three different CPW intertrack surface configurations: with the 50 nm thick silicon dioxide present between the CPW tracks (solid blue line—SiO₂). Second, measurements taken 1 hour after the silicon dioxide has been etched away from between the CPW tracks using the buffered HF solution (short-dashed green line—Si-H)—this forms a stable hydrogen-terminated surface on the 100 silicon. And finally, measurements taken after 3 months of native oxide growth on the hydrogen-terminated (100) silicon surfaces between the CPW tracks in air at room temperature (long-dashed red line—SiO_x). The small-gap CPW are connected to large CPW and contact pads via transition CPW—see insets to Fig. 4.

The curves presented in Fig. 4 are averages based on several measurements from different CPW of these types found on the SOI wafer, the standard deviations of the measurements are comparable with the values recorded for the large-gap CPW. The return losses (S_{11} and S_{22}) are less than -18 dB (SiO₂), -16 dB (Si-H), and -14 dB (SiO_x) for these measurements—plots of these data can be found in the Supplementary Information.

In order to observe the aging and hysteresis behaviour of the losses, Figure 5 shows the insertion loss (dB) of small-gap CPW systems measured after 5 years of native oxide growth—see Fig. 5(a)—and <1 hour after selective removal of the native oxide (using buffered HF) to leave a hydrogen-terminated surface—Fig. 5(b). First, the measurements taken after 5 years native oxide growth are comparable to those taken after 3-month native oxide growth—*c.f.* Fig. 4 (red-dashed curves). Second, the measurements taken <1h after selective removal of this 5-year native oxide are comparable to those taken using CPW

systems with hydrogen-terminated silicon following the removal of the LPCVD silicon dioxide—c.f. Fig. 4 (green-dashed curves). In contrast, the same measurements on large-gap CPW (not shown) revealed very little change ($<0.05 \text{ dB mm}^{-1}$) in the insertion loss when forming a hydrogen-terminated intertrack surface by removing a 5-year old native oxide—c.f. Fig. 3. This result suggests that the losses in small-gap CPW are greatly affected by the presence of a native oxide, and a hydrogen-terminated surface results in significantly lower losses than an oxide.

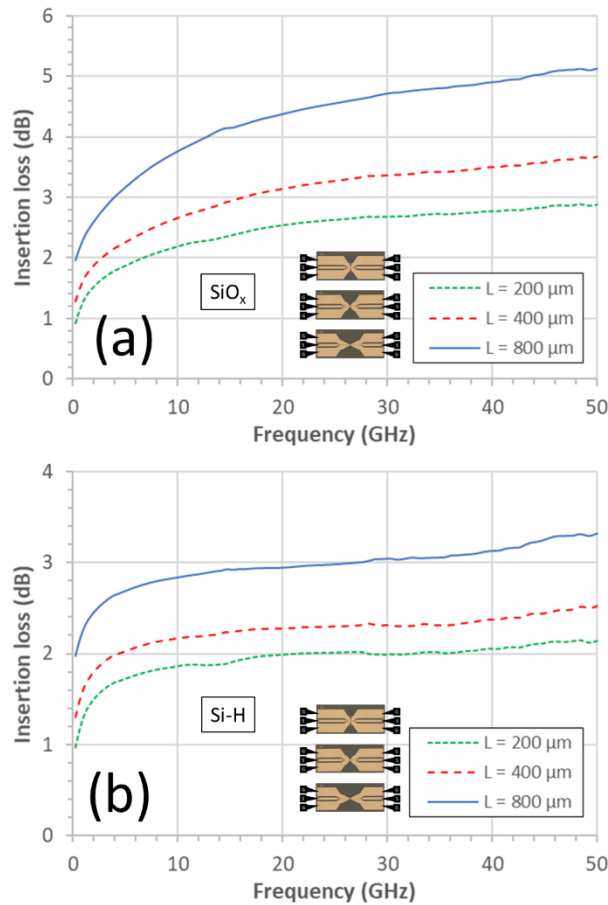


Figure 5. Measured insertion losses of the small-gap CPW systems with (a) a 5-year old native oxide (SiO_x) between the CPW metal tracks and (b) with a hydrogen-terminated silicon (Si-H) surface between the metal tracks following selective removal of the native oxide using an HF-based etch. The curves correspond to the section lengths L of the small-gap CPW: $L = 200 \mu\text{m}$ (short-dashed green curves), $L = 400 \mu\text{m}$ (long-dashed red curves), and $L = 800 \mu\text{m}$ (solid blue curve).

5. Analysis of the experimental results

5.1. Methodology of the analysis

The experimental results of the large-gap CPW enable the losses per unit length (dB mm^{-1}) to be extracted using a trivial calculation. It is then possible to subtract the modelled losses (i.e. losses due to the conductors and the substrate/layers) from these measurements to isolate the total interface losses. Any subsequent changes in losses as the result of a surface treatment can be directly associated with intertrack surface losses—based on the assumptions given above. In contrast, this is less trivial for the results obtained using the small-gap CPW systems—as they are connected to two large CPW sections via two ‘small-to-large gap’ CPW transition sections. Our methodology for the extraction of the losses in the small-gap CPW is explained in the following passage. We first remove the total losses due to the large CPW portions—obtained from the measurements on the separate large-gap CPW—from the measurements on the small-gap CPW systems. Second, we plot the resulting losses (at each frequency) as a function of small-gap CPW length ($l = 200 \mu\text{m}$, $400 \mu\text{m}$, and $800 \mu\text{m}$). This enables an extraction of the intercept loss at $l = 0$ at each frequency—and for each CPW intertrack surface configuration. This approach is analogous to the extraction of contact resistance using a ladder resistance network [36]. This intercept loss corresponds to the contribution of total losses from the two ‘large-to-small’ transition CPW. Third, subtracting these intercepts loss values (at each frequency) from the combined losses isolates the total losses uniquely in the small-gap CPW. Fourth, the modelled losses of the small-gap CPW (due to conductors and the substrate/layers) are then subtracted from the experimentally-obtained total small-gap losses to isolate the interface losses in the small-gap CPW. Finally, as with the large-gap CPW, any differences in these interface losses—due to surface treatment—are considered to be associated uniquely with the intertrack surface losses.

The total insertion losses (L_{tot}) in a CPW can be approximated by the sum of the following losses:

$$L_{tot} \cong L_{cond} + L_{sub} + L_{int} \quad (3)$$

Where L_{cond} are the losses associated with the conducting tracks, L_{sub} are the losses associated with the bulk substrate materials, and L_{int} are the losses associated with interfaces. In addition, the interface losses can be subdivided:

$$L_{int} = L_{bi} + L_{surf} \quad (4)$$

where L_{bi} are the *buried interface losses* and L_{surf} are the *intertrack surface losses*. For example, in the case of CPW on SOI material, the buried interface losses can have their origin at any silicon dioxide/silicon interface, e.g. the BOX oxide and any other layers which have been subsequently grown or deposited onto the silicon device layer surface which subsequently become situated underneath the CPW tracks.

By modelling the different CPW systems tested, it is possible to compute an estimation of the combined losses of $L_{cond} + L_{sub}$ due to conductor losses and bulk substrate losses. The modelling was performed using finite element analysis using commercial software (Comsol Multiphysics®, USA). These computed losses can be extracted from the measured losses to estimate the contribution of total interface losses L_{int} . In addition, and in a first approximation, it is reasonable to assume that any surface treatment (that does not chemically affect the Cr/Au tracks, the bulk silicon, or buried layers/interfaces) results only in a change of the intertrack surface losses L_{surf} . Thus, the difference between the measurements—before and after surface modification—will indicate a change uniquely in intertrack surface losses L_{surf} , i.e. $\Delta L_{int} = \Delta L_{surf}$. Therefore, we can write down:

$$\Delta L_{int} = \Delta L_{surf} \quad (5)$$

$$\Delta L_{surf}^{Si-H} = L_{int}^{Si-H} - L_{int}^{SiO_2} \quad (6)$$

$$\Delta L_{surf}^{SiO_x} = L_{int}^{SiO_x} - L_{int}^{SiO_2} \quad (7)$$

Using this approach, it is thus possible to: (i) isolate and plot the interface losses (L_{int}) as a function of frequency and CPW intertrack surface configuration—for both the large-gap and small-gap CPW, (ii) plot the proportion of interface losses to total losses (L_{int}/L_{tot}), (iii) plot the ratio (R_{int}) of these proportions (small-gap to large-gap)—to be able to directly compare the contributions of interface losses in the large-gap and the small-gap CPW intertrack surface losses (ΔL_{surf}), (iv) plot the proportion of the intertrack surface losses to total losses ($\Delta L_{surf}/L_{tot}$), and finally (v) plot the ratio (R_{surf}) of these last proportions (small-gap to large-gap)—to be able to directly compare the contributions of surfaces losses in the large-gap and the small-gap CPW.

However, care must be taken with comparing the attenuation losses of different systems given in decibels per unit length. It should be noted that if the ratio of two attenuation coefficients of the transmission lines is plotted unitless in dB dB⁻¹ then this is not equivalent to the ratio of the linear losses. Thus, to compare losses in different measurements, the ratio of the *lost* powers R_{lp}^{21} (at a given unit length) in the two CPW (superscripts 1 and 2) of each measurement can be plotted. R_{lp}^{21} can be written in terms of the attenuation coefficients of the lines (α_{dB}^1 and α_{dB}^2) as:

$$R_{lp}^{21} = \frac{1 - e^{-\frac{-\ln 10}{10} \alpha_{dB}^2}}{1 - e^{-\frac{-\ln 10}{10} \alpha_{dB}^1}} \quad (8)$$

where system 1 is more lossy than system 2, i.e. $|\alpha_{dB}^1| > |\alpha_{dB}^2|$, meaning $R_p < 1$. Again, the superscripts of the attenuation coefficients refer to the individual lossy system, not exponentiation. See Supplementary Information for the reasoning behind, and the derivation of, Eq. (8).

5.2. Interface losses in large-gap CPW

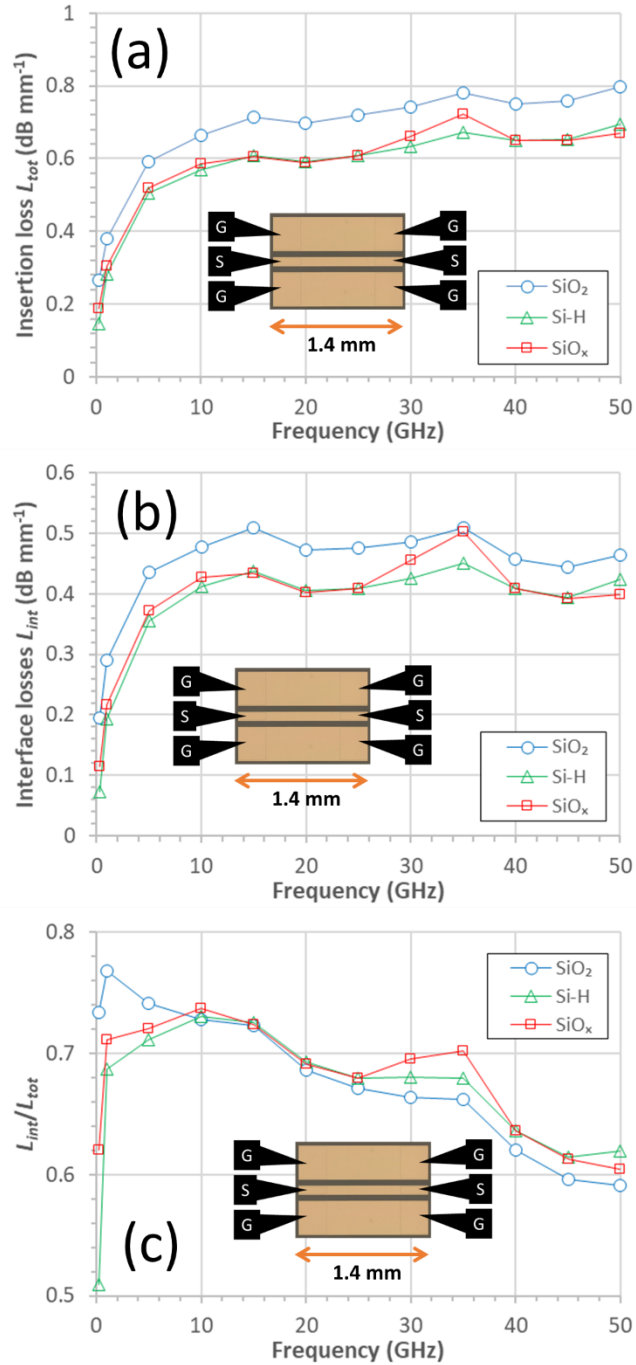


Figure 6. The insertion and interface losses in large-gap CPW. (a) The total insertion losses L_{tot} (dB mm⁻¹), (b) the interface losses L_{int} (dB mm⁻¹), and (c) the ratio of the interface losses to total losses (L_{int}/L_{tot}). Results are given for: a silicon dioxide layer present between the CPW tracks (open blue

circles—SiO₂), a hydrogen-terminated (100) silicon surface between the CPW tracks (open green triangles—Si-H), and a native oxide grown on the Si-H surface between the CPW tracks (open red squares—SiO_x). The CPW have a length L of 1.4 mm, a signal line width s equal to 100 μm , and a signal-to-ground gap width g equal to 63.5 μm .

Figure 6 shows the insertion and interface losses in the large-gap CPW. Fig. 6(a) shows the insertion losses (dB mm⁻¹) from 0.25 GHz to 50 GHz for three different intertrack surface configurations. First, the insertion losses (per unit length) are comparable with similar CPW in the literature. It can be observed that the HF treatment leads to a reduction of the insertion losses by approximately 0.1 dB mm⁻¹ over the whole measurement range (green triangles). After 3 months of native oxide growth between the tracks, a very slight change in the losses is observed. Fig 5(b) shows the extracted interface losses in the large-gap CPW—these have been obtained by removing the modelled conductor and dielectric losses. Fig. 5(c) shows a plot of the ratio of the interface losses to the total insertion losses. It is seen that the ratio is approximately similar for the three intertrack surface configurations—apart from at lower frequencies, where the interface loss contribution is higher with the presence of the silicon dioxide between the tracks.

5.3. Interface losses in small-gap CPW

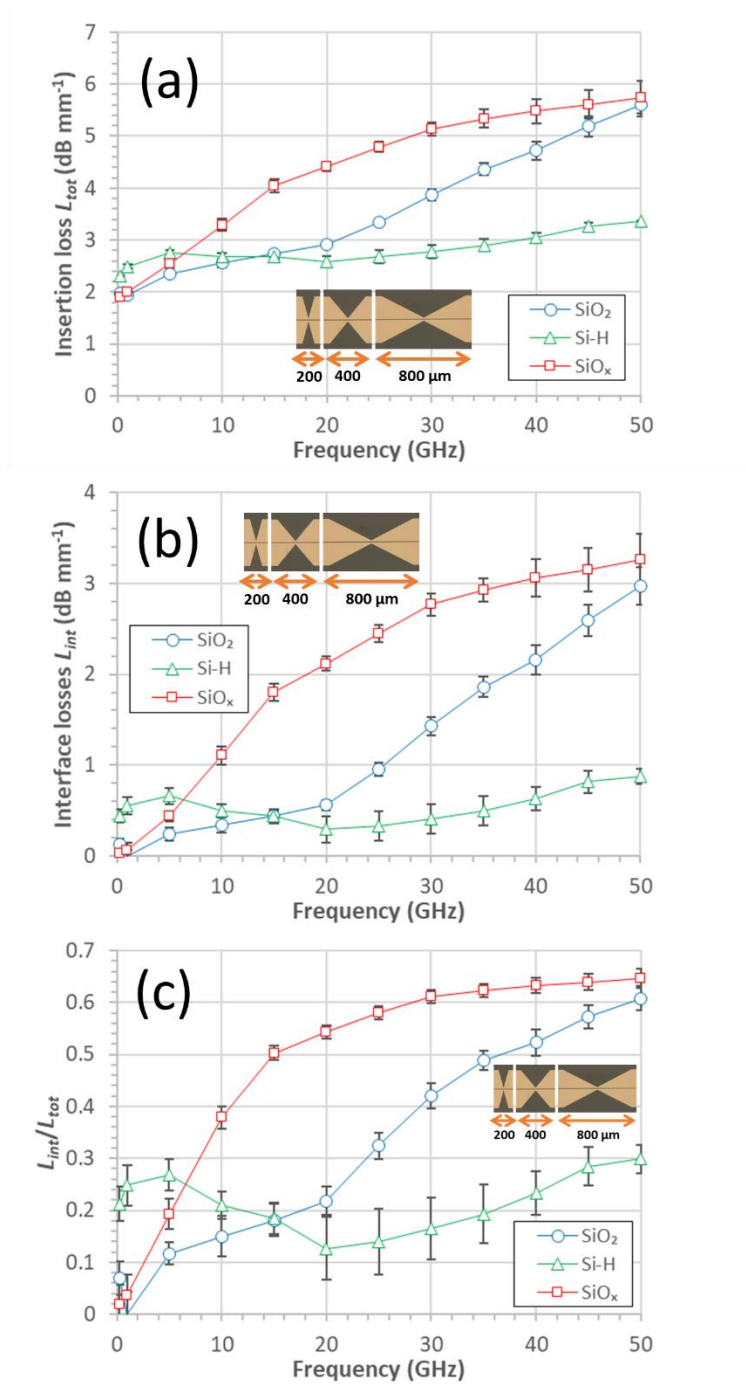


Figure 7. The insertion and interface losses in small-gap CPW. (a) The total insertion losses L_{tot} (dB mm^{-1}), (b) the interface losses L_{int} (dB mm^{-1}), and (c) the ratio of the interface losses to total losses (L_{int}/L_{tot}). Results are given for: a silicon dioxide layer present between the CPW tracks (open blue circles— SiO_2), a hydrogen-terminated (100) silicon surface between the CPW tracks (open green

triangles—Si-H), and a native oxide grown on the Si-H surface between the CPW tracks (open red squares—SiO_x). The small-gap CPW have a signal line width s equal to 2 μm , and a signal-to-ground gap width g equal to 2.5 μm .

Figure 7 shows the result of the extraction of the insertion losses and the interface losses in the small-gap CPW. Fig. 7(a) shows the extracted insertion losses (dB mm^{-1}) of uniquely the small-gap CPW from 0.25 GHz to 50 GHz for three different intertrack surface configurations. Overall, the insertion losses are higher than for the large-gap CPW—this has been previously seen [37]. It can be observed that the HF treatment again leads to a reduction of the insertion losses—but this time by approximately 2.5 dB mm^{-1} at 50 GHz (green triangles). After 3 months of native oxide growth between the tracks, a relatively large increase in the losses is observed—the losses due to the presence of the native oxide being larger than for the silicon dioxide when the measurement frequency is >10 GHz. Fig 7(b) shows the extracted interface losses in the small-gap CPW—these have been obtained using the methods described above in Section 5.1. Fig. 7(c) shows a plot of the ratio of the interface losses to the total insertion losses for the small-gap CPW. In stark contrast to the large-gap CPW—*c.f.* Fig. 6(c)—the contributions of the interfaces losses for the small-gap CPW depend strongly on the intertrack surface configuration. They are noticeably much lower for the intertrack hydrogen-terminated silicon surface (green triangles) compared to the two oxides (silicon dioxide and native oxide). The interface loss contribution is also higher for the native oxide (red squares) than the silicon dioxide (blue circles) in the small-gap CPW. In order to obtain Fig. 7(a), which is based on the measurement of 3 lengths of small-gap CPW, it should be noted that at all frequencies and surface conditions, when the total losses are plotted as a function of small-gap CPW length (as described in Section 5.1), the data is linear with a coefficient of determination (R^2) equal to near unity enabling an accurate extraction of the intercept losses at $l = 0$, as described above..

Let us now consider and compare the contributions of the intertrack surface losses in the different intertrack surface configurations for the large-gap and the small-gap CPW.

5.4. Intertrack surface losses in large-gap and small-gap CPW

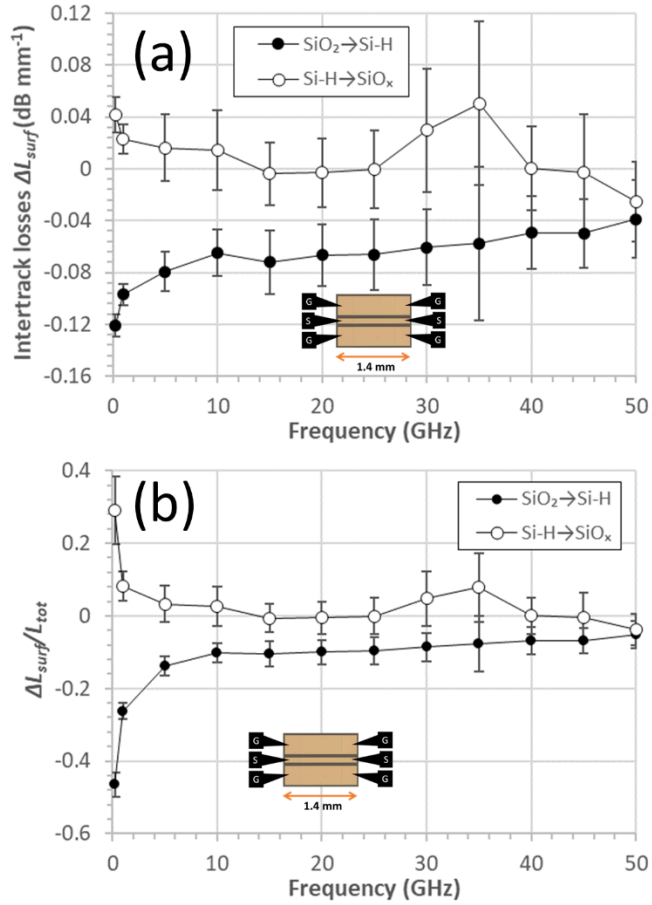


Figure 8. The intertrack surface losses in large-gap CPW. (a) The change in losses due to intertrack surface losses ΔL_{surf} (dB mm⁻¹) and (b) the ratio of the change of intertrack surface losses to the total losses ($\Delta L_{surf}/L_{tot}$). Results are given for the change between a silicon dioxide and a hydrogen-terminated silicon surface between the CPW tracks ($\text{SiO}_2 \rightarrow \text{Si-H}$: filled circles), and the change from a

hydrogen-terminated silicon surface to a native oxide between the CPW tracks ($\text{Si-H} \rightarrow \text{SiO}_x$; open circles). The CPW have a length L of 1.4 mm, a signal line width s equal to $100 \mu\text{m}$, and a signal-to-ground gap width g equal to $63.5 \mu\text{m}$.

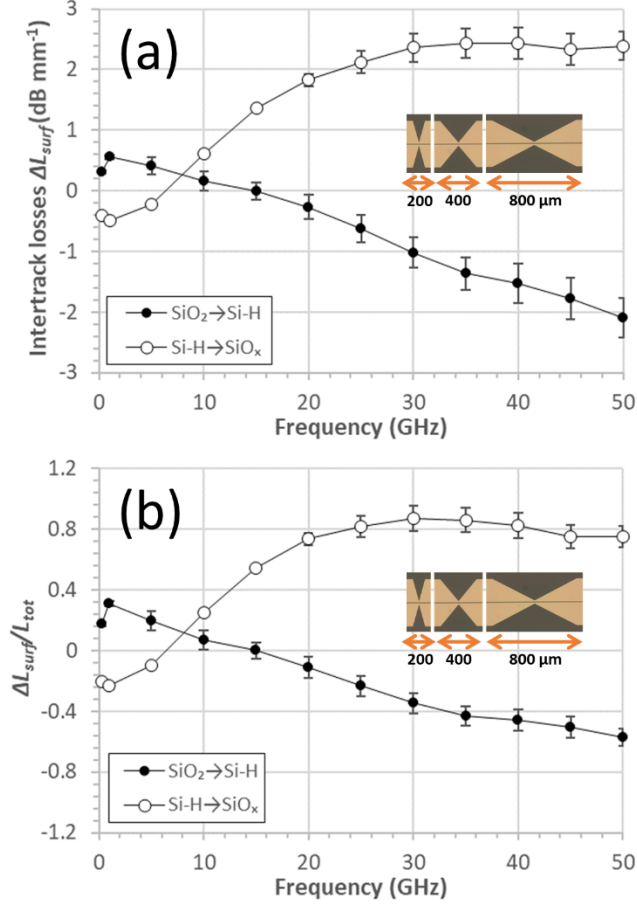


Figure 9. The intertrack surface losses in small-gap CPW. (a) The change in losses due to intertrack surface losses ΔL_{surf} (dB mm⁻¹) and (b) the ratio of the change of intertrack surface losses to the total losses ($\Delta L_{surf}/L_{tot}$). Results are given for the change between a silicon dioxide and a hydrogen-terminated silicon surface between the CPW tracks ($\text{SiO}_2 \rightarrow \text{Si-H}$: filled circles), and the change from a hydrogen-terminated silicon surface to a native oxide between the CPW tracks ($\text{Si-H} \rightarrow \text{SiO}_x$: open circles).

The small-gap CPW have a signal line width s equal to $2\ \mu\text{m}$, and a signal-to-ground gap width g equal to $2.5\ \mu\text{m}$.

The intertrack surface losses (ΔL_{surf}) and their proportional contribution compared to the total losses ($\Delta L_{surf}/L_{tot}$) are shown in and for the large-gap CPW (Figure 8) and small-gap CPW (Figure 9). If we first compare Fig. 8(a) to Fig. 9(a), the data being ratios, it is apparent that the intertrack surface losses play a more important role for small-gap CPW than for large-gap CPW. In the case of the small-gap CPW—Fig. 9(a)—the change of intertrack surface configuration from silicon dioxide to hydrogen-terminated silicon (filled circles) and from hydrogen-terminated silicon to native oxide (open circles) leads to large changes in the losses. Fig. 8(b) and Fig. 9(b) plot these changes as a ratio of the total losses. Again, this proportion is larger for the small-gap CPW. We are now able to quantitatively compare the contributions of the intertrack surface losses of the two types of CPW if we plot the ratios of these results—this is shown in Figure 10.

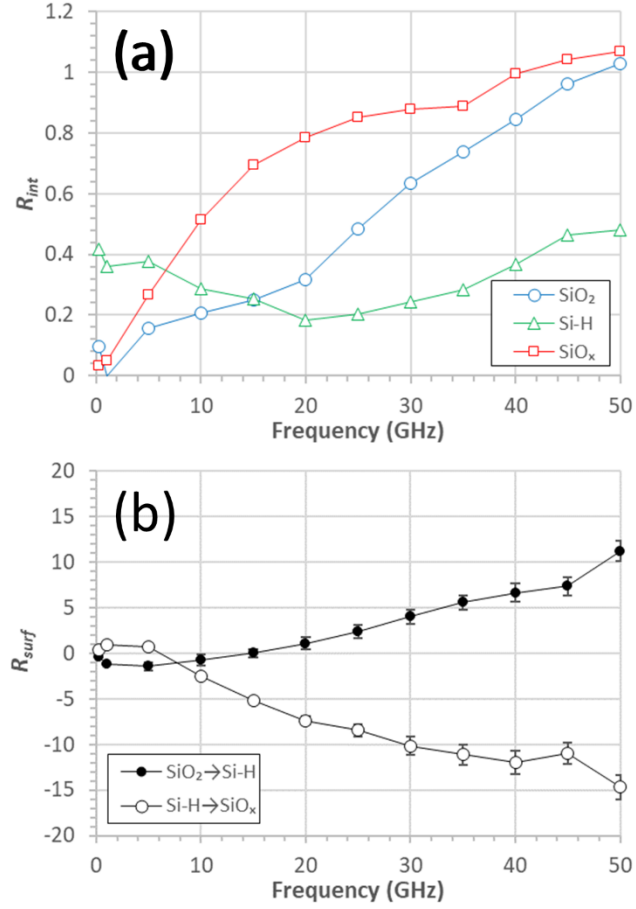


Figure 10. Comparison of the intertrack surface losses in large-gap and small-gap CPW. (a) The ratio R_{int} corresponds to $(L_{int}^s/L_{tot}^s)/(L_{int}^l/L_{tot}^l)$. (b) The ratio R_{surf} corresponds to $(\Delta L_{surf}^s/L_{tot}^s)/(\Delta L_{surf}^l/L_{tot}^l)$ —where the superscripts refer to small-gap (s) and large-gap (l). For (a) the open blue circles correspond to a 50 nm thick silicon dioxide (SiO_2) present between the tracks, the open green triangles correspond to a hydrogen-terminated silicon surface (Si-H) between the CPW tracks, and the open red squares correspond to a native oxide (SiO_x) between the tracks. For (b), the filled circles correspond to the change between a silicon dioxide and a hydrogen-terminated (100) silicon surface between the CPW tracks ($\text{SiO}_2 \rightarrow \text{Si-H}$), and the filled circles correspond to the change from a hydrogen-terminated silicon surface to a native oxide between the CPW tracks ($\text{Si-H} \rightarrow \text{SiO}_x$).

Figure 10 shows the comparison of the intertrack surface losses in the large-gap and small-gap CPW. The plots in Fig. 10(a) enable us to compare the contributions of the interface losses in the two types of CPW using the ratio R_{int} . The contribution of all interface losses (beneath and between the CPW tracks) is smaller for small-gap CPW in all intertrack surface configurations—except for the native oxide surface above 40 GHz where their contributions are approximately the same in the two sizes of CPW. The plots in Fig. 10(b) plot the ratio R_{surf} which directly compares the contribution of the surface losses in small-gap and large-gap CPW. For example, at 50 GHz, the contribution of the surface losses is an order of magnitude larger in the small-gap CPW than the large-gap CPW—when changing the CPW intertrack surface from silicon dioxide to a hydrogen-terminated silicon (filled circles) and from hydrogen-terminated silicon to a 3-month-old native oxide (open circles). Let us now discuss the physical mechanisms involved and consider reasons why this should be so.

6. Discussions

6.1. Comparisons of results with measurements on comparable CPW

Pfeifer *et al* [38] measured losses in Cr/Au CPW ($s = 20 \mu\text{m}$) on silicon wafers with and without a 200 nm thick silicon dioxide layer. They concluded that the inclusion of the silicon dioxide layer increases losses due to charge accumulation and inversion at the silicon dioxide/silicon dioxide interface caused by fixed oxide charges. However, they did not remove the silicon dioxide selectively from between the tracks. Ponchak [37] studied losses in CPW on high-resistivity silicon as a function of metallization dimensions, observing that a smaller signal width significantly increases losses.

Wu *et al* [39,40] and Gamble *et al* [41] conducted studies on the intertrack surface losses in CPW on silicon wafers. Wu *et al* [39] incorporated a silicon dioxide into CPW to reduce intertrack surface losses. Wu *et al* [40] and Gamble *et al* [41] studied losses and considered their mechanisms in large-gap CPW patterned on silicon. They showed that at 30 GHz and for CPW ($w = 40 \mu\text{m}$ $s = 70 \mu\text{m}$) losses

decrease from $\sim 1.8 \text{ dB mm}^{-1}$ to 0.3 dB mm^{-1} when a 100 nm thick LPCVD oxide is selectively removed in the CPW gap. Based on ideas proposed by Reyes *et al* [42], they suggested that the fixed charge in the oxide cause electrons to be attracted to the Si/SiO₂ interface which forms an inversion layer between the signal and ground tracks of the CPW—the presence of these carriers would result in increased losses due free carrier absorption near the surface. They also suggested that selective removal of the silicon dioxide—using HF—uniquely between the metallized CPW tracks removes the fixed positive oxide charges and thus the minority carrier inversion layer between the CPW tracks explaining their observed lower losses. Schollhorn *et al* [14] studied loss mechanisms in micropatterned CPW on oxidized (200 nm) silicon ($\rho > 1000 \text{ } \Omega \text{ cm}$). They studied 50 Ω CPW having signal track widths s equal to 20 μm and 45 μm using 1 μm thick aluminium tracks. First, they observed larger attenuation on CPW having smaller signal track width. Second, they observed lower substrate losses for higher resistivity silicon substrates. They identified bias-dependent interface losses at the oxide/silicon interface under the metallisation. These losses were higher for inversion layers than accumulation layers in p-type silicon—hypothesized to be due to the larger electron mobility in silicon. The nature of the metallization meant that they were not able to remove the oxide between the tracks using HF-based wet etch solutions. Lederer and Raskin [43] considered the contributions of loss mechanisms in CPW and microstrip (MS) transmission lines on oxidized silicon. They found that CPW on a thermal oxide (SiO₂) on high-resistivity ($>5000 \text{ } \Omega \text{ cm}$) silicon was more sensitive to DC biasing and its polarity than MS—implying that buried interface charges (and their absorption) underneath tracks were at the origin of a significant proportion of the losses in this system. Yuhang *et al* [44] proposed lower-loss a ‘V-groove’ CPW based on SOI wafers. Using CPW having a signal-to-ground gap width of 30 μm . They demonstrated lower insertion losses by removing—using selective etching—the CVD oxide and part of the silicon device layer underneath the metal tracks. They observe that the insertion losses can be reduced from $>2 \text{ dB mm}^{-1}$ to $\sim 1 \text{ dB mm}^{-1}$. The findings here suggest that the reduced losses observed by Yuhang *et al* [44] have, at least in part, their origin at interfaces between the tracks. Finally, in terms of losses associated with a buried layer, Neve *et al* [45]

showed that a buried trap-rich layer could reduce losses of CPW on silicon having a resistivity in the range 2-5 k Ω cm.

6.2. The different CPW intertrack surfaces

It has long been known that energy band bending at the surface of a semiconductor [46] (due to deposition of materials and surface treatments) causes a modification of free carriers (electrons or holes) in proximity to the surface compared to the bulk. In CPW on semiconductors, such carriers can contribute to losses via free carrier absorption. To understand the origin of the losses in the three different intertrack surface configurations here, we need to look at these surfaces and their properties.

6.2.1. Silicon dioxide/ silicon

If an oxide is thermally- grown or deposited onto the surface of weakly-doped crystalline silicon, it is known that fixed oxide charges [47,48] can lead to the formation of a ‘natural’ inversion layer in the silicon near to the silicon-oxide interface [49]. If the silicon has a light p-type background, as is the case here, then the fixed oxide charges—which are known to be positive—will result in an inversion layer of electrons near the silicon dioxide-silicon interface. For LPCVD oxides, Ang *et al* [50] showed that the oxide fixed charge density is in the mid- 10^{11} cm $^{-2}$. Buchanan *et al* [51] observed trapped positive charge as high as $\sim 10^{12}$ cm $^{-2}$ in CVD-grown silicon dioxide films on silicon. Using p-type (100) silicon, Gaid and Kasprzak [52] measured a distributed oxide charge of 1.5×10^{15} cm $^{-3}$ and an interface charge of 1.1×10^{10} cm $^{-2}$ for a CVD oxide. Lee *et al* [53] showed that the interface state density of CVD oxides is in the low- 10^{11} cm $^{-2}$ eV $^{-1}$ following high-temperature annealing. The mobility of carriers in these inversion layers has been studied by Sun and Plummer [54]. They showed that the mobility of the carriers in the inversion layer depends on the background doping of the silicon and the oxide charge density.

6.2.2. Hydrogen-terminated silicon

Let us consider the hydrogen-terminated (100) silicon surface resulting from a hydrofluoric acid-based treatment [55]—often used for temporary surface passivation [56] via the formation of a nonpolar Si-H bond. In terms of the stability of the hydrogen termination, following exposure to the HF-based solution, the (100) silicon surface between the metal tracks becomes hydrogen-terminated with a high surface coverage [30] and high degree of stability [31]. Using Auger electron spectroscopy, Kluth and Maboudian [57] observed a stable Si-H surface up to >100 hours after NH_4F treatment of a (100) silicon surface. In terms of the electrical properties of the Si-H surface, Weinberger *et al* [58] and Yablonovitch *et al* [59] have demonstrated the passivation of electrical sites on the surface of silicon to $<10^{10} \text{ cm}^{-2}$ using fluorination by a number of techniques, including exposure to HF. Using surface photovoltage measurements, Angermann [60] showed that the surface Fermi level position was near zero for p-type silicon treated with an NH_4F -based solution. Using moderately doped (p-type and n-type) silicon Huang and Lau [61,62] observed that and dilute HF (<5%) treatment of silicon surface could achieve near-flatband surfaces—although others have observed Fermi-level pinning in HF-treated silicon surfaces [63,64]. Recently, using thin silicon layers, Peng *et al* [65] found that hydrogen-termination results in surface ‘donor-like’ states in the $10^{11} \text{ cm}^{-2} \text{ eV}^{-1}$ range.

6.2.3. Native oxide on a hydrogen-terminated surface

Let us consider the native oxide formed on a hydrogen-terminated silicon surface. When a hydrogenated silicon surface—obtained using an HF-based solution [55]—is exposed to oxygen in the air at room temperature, a thin native oxide slowly grows on the surface. Raider *et al* [32] showed that it takes 5 weeks to grow a native oxide having a thickness of 1.8 nm in air at room temperature following an HF ‘etch’—indeed, they observed a much more rapid oxidation on cleaved silicon surfaces. According to Morita *et al* [66], the native oxide thickness on moderately doped (100) silicon wafers, which had been treated with an aqueous HF solution before exposure to humid air ($23.7^\circ\text{C}/\text{RH}=42\%$) [66], varies from ~0.2 nm to ~0.8 nm over a period of ~2 to 3 months. Graf *et al* [67] studied native oxide growth on HF-

treated p-type (100) silicon wafers. They report a 0.8 nm thick SiO₂ layer having formed after 6 months exposure of the silicon surface to air. They reported very little native oxide growth (<0.1 nm) in the first day after HF treatment and exposure to air. In terms of the composition of a native oxide allowed to grow on a silicon surface at room temperature for several months following an HF treatment, Philipe and Taft [68] showed that the oxide contains no SiO₂, but is composed of SiO_x (1 ≤ x < 2). Renaud *et al* [69] later showed that the interface phase between this native oxide and silicon is highly disordered.

In terms of electrical properties, Shimizu and Munakata [70] showed that the surface photovoltage varies considerable for lower doped silicon during oxide regrowth. They attributed this to the influence of the fixed oxide charges on the surface depletion. Angermann *et al* [71] showed that the surface state distribution D_{it} of p-type silicon (270 Ω nm and <111>) increases from $4 \times 10^{11} \text{ eV}^{-1} \text{ cm}^{-2}$ to $2.45 \times 10^{12} \text{ eV}^{-1} \text{ cm}^{-2}$ over a period of 16 days of native oxide regrowth following an HF treatment—following a $D_{it} = 6.52 \times 10^{11} t^{0.226}$ relationship if t is in hours. Mizsei [72] measured the surface potential of ultra-thin silicon dioxide layers—finding a correlation between the electrical properties of the surface and the growth properties. Mizsei [73] has also shown that the bulk doping density of the silicon determines the if the free carriers at the silicon/native oxide interface are in accumulation, depletion, or inversion—for p-type silicon, the surface is in inversion.

6.3. Losses due to free carrier absorption in silicon

The absorption coefficient of free carriers in a semiconductor can be modelled based on the Drude model of conduction [74] and has proved to be a reasonable approximation [75,76]. The real and imaginary parts of the complex permittivity $\varepsilon = \varepsilon' - j\varepsilon''$ are given by:

$$\varepsilon' = \varepsilon_{Si} \left(1 - \frac{\omega_p^2 \tau^2}{1 + \omega^2 \tau^2} \right) \quad (9)$$

$$\varepsilon'' = \varepsilon_{Si} \frac{\omega_p^2 \tau}{\omega(1 + \omega^2 \tau^2)} \quad (10)$$

Where ω is the angular frequency ($\omega = 2\pi f$), ϵ_{Si} is the dielectric constant of silicon, τ is the average scattering time, and ω_p is the plasma frequency which is given by:

$$\omega_p = \sqrt{\frac{nq^2}{m^* \epsilon_{Si}}} \quad (11)$$

where n is the carrier density, q is the elementary charge, and m^* is the effective mass of the carriers. The average scattering time τ is given by:

$$\tau = \frac{m^*}{q} \mu \quad (12)$$

where μ is the mobility of the charge carriers.

The dielectric constant of silicon ϵ_{Si} , the elementary charge q , the mass of the electron m_e , the vacuum permittivity ϵ_0 , and the speed of light are taken to be: 11.9, 1.6×10^{19} C, 9.11×10^{-31} kg, 8.85×10^{-12} Fm⁻¹, and 3×10^8 ms⁻¹, respectively. The following values of carrier mobility and effective mass are used for lightly doped silicon: (electrons: 1500 cm² V⁻¹ s⁻¹ and $0.26m_e$) and (holes: 450 cm² V⁻¹ s⁻¹ and $0.37m_e$). The effective masses are those used in conductivity calculations--although it should be noted that the mobilities in surface inversion layers are modified [54].

Finally, the absorption coefficient α (per unit length) is given by:

$$\alpha = \frac{\omega}{c} \text{Im} \sqrt{\epsilon' - j\epsilon''} \quad (13)$$

Where $\text{Im} \sqrt{\epsilon' - j\epsilon''}$ is the imaginary part of the square root of the complex permittivity.

Figure 11 shows plots of the calculated absorption coefficient α of free carriers (Fig. 11(a) – electrons and Fig. 11(b) – holes) in silicon as a function of frequency and free carrier density.

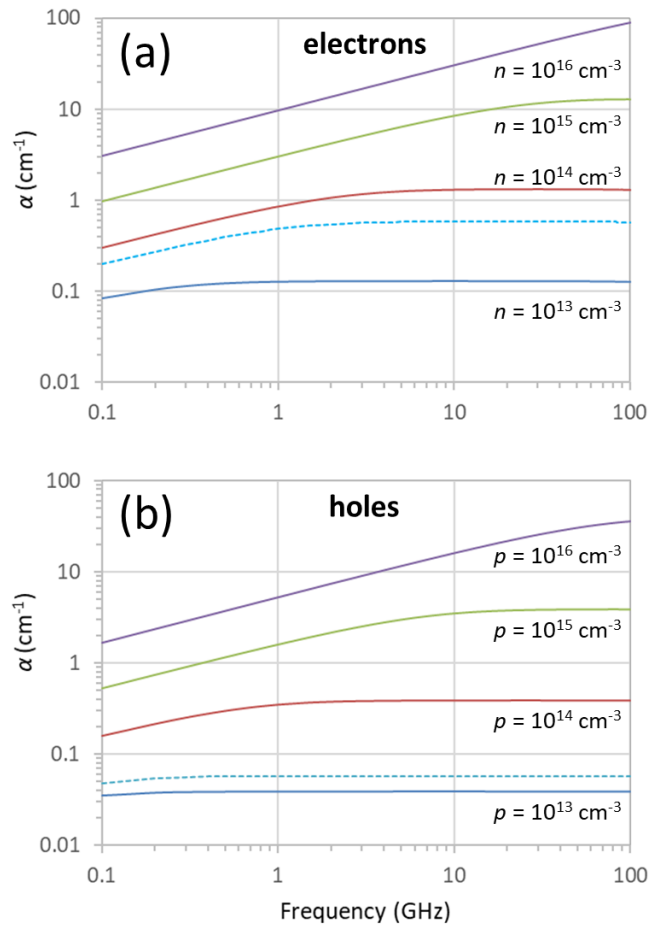


Figure 11. Plots of the calculated absorption coefficient α versus frequency for different values of carrier density n/p of (a) electrons and (b) holes. The dashed light blue line in (a) shows the absorption coefficient for a maximum electron density ($4.5 \times 10^{13} \text{ cm}^{-3}$) generated by background lighting. The dashed light blue line in (b) shows the absorption coefficient for the maximum hole background density ($1.46 \times 10^{13} \text{ cm}^{-3}$) of the bulk silicon-on-insulator wafers used for the study.

There are several observations which can be made from Fig. 11 in the context of losses in CPW. First, for both carriers (electrons and holes), the absorption coefficient increases with frequency. Second, the absorption coefficient is larger for electrons than holes at all frequencies—this should be apparent in CPW on semiconductor surfaces which favour either electron or hole accumulation, depletion, or

inversion. Third, for both types of carriers, at higher frequency, the change in absorption coefficient is more sensitive to a change in free carrier density, i.e. at higher frequency, the losses associated with free carrier absorption in CPW will be sensitive to changes in the free carrier density where the electric field energy is high, i.e. between the tracks. Finally, the sensitivity of the absorption coefficient to variations in the carrier density suggests that gains are to be made in terms of losses by reducing free carrier presence where electric field energy density is high.

We are now in a position to tentatively link the experimentally-observed changes in the attenuation coefficient of the line $\Delta\alpha_{dB}$ (assumed to be due to a change in free carrier absorption) with the computed changes in the absorption coefficient of silicon due to excess free carriers Δn , i.e. $\Delta\alpha_{dB} \propto \Delta\alpha_{Np} \cong \Delta\alpha = f(\Delta n)$. Let us consider the experimental results obtained using the small-gap CPW. With reference to Fig. 9(a), the change in surface losses at 50 GHz is ~ 2 dB mm⁻¹ when hydrogenating or oxidizing the intertrack silicon surface. This is equivalent to a change in the absorption coefficient α of ~ 23 cm⁻¹. It can be seen from Fig. 11(a) that at 50 GHz this would correspond to an approximate change of $\sim 2 \times 10^{15}$ cm⁻³ free carriers—an electron inversion layer [54,77]—near the surface. When multiplied by the Debye length, this results in a surface charge equal to $\sim 2.3 \times 10^{11}$ cm⁻²—a value which agree well with the value calculated analytically by Deal et al [49]. This values is also comparable with that given by Wu *et al* [39] and Gamble *et al* [41]. The free-carrier loss modelling and our experimental observation a suggest that the free-charge density near the hydrogen-terminated silicon surface between the tracks is of the order of the background doping density of the silicon $\sim 1.5 \times 10^{13}$ cm⁻³. We can now understand the schematic representation of the charges given in Fig. 2. Using the empirical relationship given in Sun and Plummer [54], the effective electron mobility in the inversion layer is calculated to be ~ 1000 cm² V⁻¹ s⁻¹ for $N_A = 1.47 \times 10^{13}$ cm⁻³ and a surface charge equal to 2.3×10^{11} cm⁻²—this does not significantly change the absorption coefficient.

Finally, as most microwave measurements are performed in a lit room, we will consider and compute the effect of a low background irradiance on the carrier concentration at the surface of the silicon between the tracks. This irradiance of our weak background lighting is calculated to be $60 \mu\text{W cm}^{-2}$. This level of irradiance leads to a small excess carrier concentration which depends on the surface of the silicon—due to the change in surface recombination velocity. For hydrogen-terminated silicon the average excess carrier concentration within a Debye length ($\sim 1 \mu\text{m}$ – see Supplementary Information) is $4.4 \times 10^{13} \text{ cm}^{-3}$, for a native oxide ‘grown’ on an initially hydrogen-terminated silicon surface for several months in air at room temperature, the average excess carrier concentration within a Debye length is $3 \times 10^{12} \text{ cm}^{-3}$ —see Supplementary Information for details of the calculation. It should be noted that higher irradiance incident light can modify losses in CPW (see Supplementary Information) but study have found that irradiances in the range $0.2\text{-}3 \text{ W cm}^{-2}$ do not alter the observed losses [78,79].

6.4. Estimation of the contribution of intertrack surface losses

There are examples in the literature of attempts to characterize and model the contribution of the intertrack surface losses. Barends *et al* [80] pointed out the importance of surface losses on a ‘bare’ silicon substrate. They showed that these losses increase by a factor of ~ 8 when reducing the CPW signal track width from $100 \mu\text{m}$ to $1 \mu\text{m}$. They proposed and demonstrated the technological solution of etching the silicon away between the tracks where the electric field is highest. Wenner *et al* [17] were surprised to find the substrate-air losses contribute considerably to total losses in CPW compared with microstrip. They computed the ‘substrate-air’ losses to be ~ 3 times larger for small gap ($2 \mu\text{m}$) CPW compared to large-gap ($20 \mu\text{m}$) CPW. The role of amorphous and native oxides on intertrack surface losses in superconducting CPW resonators has been pointed out [81,82] which has led to work concerning the modelling of interface losses. Murray *et al* [83] developed an analytical model based on electrostatics to compute the contribution (termed participation P) of ‘surface-air’ losses to the total losses P_{sa} . To do this they

computed the ratio of the electric field energy, residing in a small volume having thickness δ at the substrate surface between the tracks of planar electrodes U_{sa} to the total electric field density U_{tot} . Figure 12 shows a schematic diagram of the electric field lines in the case of two CPW having different gap sizes. The important point is that the intertrack losses are associated with the proportion of the total energy of the electric field near to the surface (red circles)—this energy ratio is not the same as the gap size is shrunk.

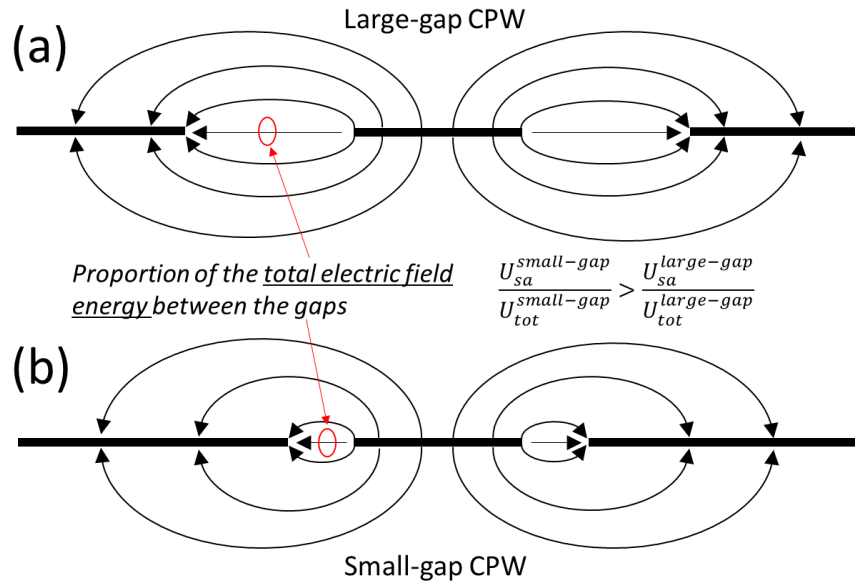


Figure 12. Schematic diagram showing electric field lines associated with (a) ideal large-gap and (b) small-gap CPW. The red circles indicated the proportion of the total electric field *energy* residing in a small volume of space between the CPW tracks. This energy proportion is not the same as the gap distances are diminished. Smaller CPW have a higher proportion of electric field energy (compared to the total electric field energy) between the gaps than large-gap CPW.

This ratio $P_{sa} = U_{sa}/U_{tot}$ is calculated to be [83]:

$$P_{sa} \left(\frac{\delta}{a} \right) \approx \frac{\varepsilon_c}{(\varepsilon_{sub} + 1)} \frac{1}{2(1-k)K(k')K(k)} \left(\frac{\delta}{a} \right) \left\{ \ln \left[4 \left(\frac{1-k}{1+k} \right) \right] - \frac{k \ln(k)}{(1+k)} + 1 - \ln \left(\frac{\delta}{a} \right) \right\} \quad (14)$$

Where $k = a/b$, $k' = \sqrt{1 - (a/b)^2}$, $K(k)$ and $K(k')$ are the elliptic integrals of k and k' , ε_c and ε_{sub} are the relative permittivities of the surface layer and the substrate and a and b can be equated to the dimensions of a CPW to be: $w = 2a$ and $s = b - a$. Their calculations agree well with a numerical FEM analysis [17]. This model predicts that there are proportionally higher losses associated with the surface as the dimensions of CPW shrink.

By using the coplanar dimensions in the experimental work here, the contribution of the intertrack surface losses in CPW can be computed. Figure 13 shows a calculation of the participation of the surface-air losses P_{sa} as a fraction of the total losses in coplanar waveguide based on the above equation. The computed loss participation is given as a function of surface depth δ as explained above. The CPW dimensions used for the calculation correspond to the large-gap CPW (filled black circles) and small-gap CPW (open black circles) used to obtain the experimental results. The ratio of the loss participations $P_{sa}^{small} / P_{sa}^{large}$ is shown by open diamonds. The model predicts that the surface-air loss participation is larger for the small-gap CPW. In the case if we consider a surface depth range of 0.1-1 μm , the model also approximately predicts the ratio of the surface losses R_{surf} observed experimentally above 20 GHz—see *c.f.* Fig. 10(b). Incidentally, the Debye length of the silicon at this doping density is $\sim 1 \mu\text{m}$ —see the Supplementary Information.

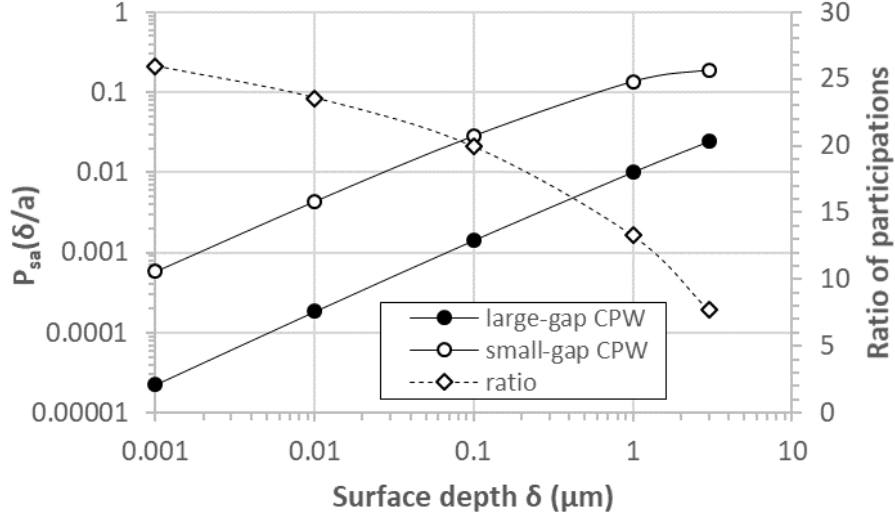


Figure 13. Calculation of the participation of the surface-air losses P_{sa} as a fraction of the total losses in coplanar waveguide. The loss participation is given as a function of surface depth δ . The CPW dimensions used for the calculation correspond to the large-gap CPW (filled black circles) and small-gap CPW (open black circles) used to obtain the experimental results. The ratio of the loss participations $P_{sa}^{small}/P_{sa}^{large}$ is shown by open diamonds. The values of ϵ_c and ϵ_{sub} are 5 and 11.7. The values of the elliptic integrals $K(k)$ and $K(k')$ were evaluated numerically to be 1.59 and 2.84 for the large-gap CPW and 1.63 and 2.4 for the small-gap CPW. The lines linking the data points are not analytical function fits.

7. Conclusions

In the case of large-gap CPW (signal track width $s = 100 \mu\text{m}$ and track spacing $g = 63.5 \mu\text{m}$) patterned on silicon-on-insulator (SOI) wafers, selective removal of the silicon dioxide from between the CPW tracks (using buffered HF) results in some reduced losses—e.g. from 0.79 dB mm^{-1} to 0.69 dB mm^{-1} at 50 GHz. Subsequently, a native oxide growth on the hydrogen-terminated (100) silicon surface between the CPW tracks results in no significant change in losses. In the case of small-gap CPW ($s = 2 \mu\text{m}$, $g = 2.5 \mu\text{m}$) of patterned onto SOI, selective removal of the silicon dioxide from between tracks reduces losses

considerably—e.g. from 5.6 dB mm⁻¹ to 3.4 dB mm⁻¹ at 50 GHz. However, native oxide regrowth over a period of months on the silicon surface between the CPW tracks leads to a significant increase in losses to 5.8 dB mm⁻¹ at 50 GHz. The removal of this native oxide using an HF-based solution, even after years of growth, demonstrates that the losses revert to their low value observed after removal of the thin film silicon dioxide—this proves the role of the oxide (thin film or native) in the loss mechanism. We suggest that technologies employing miniature CPW on silicon should take intertrack surface losses into account. The native oxide should be routinely removed if possible, or fabrication processes should incorporate stable surface passivation of the silicon surface specifically between the CPW tracks to avoid native oxide growth following manufacture. Finally, the observed sensitivity of the miniature CPW characteristics to the intertrack surface state suggests that miniaturization could be beneficial for sensitivity enhancement in CPW-based biosensing applications [7,84].

Acknowledgements

The authors would like to thank the following people for their invaluable technical input: F. Vaurette for help with the electron beam lithography, A. Fattorini for help with the metallization, and D. Desremes for help with the AFM measurements. This work was financially supported by a French ‘Equipex’ project ‘Excelsior’ and partially supported by the French Renatech network. The digital microscope was purchased within the ‘TIPTOP_1’ project (ANR-16-CE09-0029).

ORCID iDs

Steve Arscott <https://orcid.org/0000-0001-9938-2683>

References

- [1] Wen C P 1969 Coplanar Waveguide: A Surface Strip Transmission Line Suitable for Nonreciprocal Gyromagnetic Device Applications *IEEE Trans. Microw. Theory Tech.* **17** 1087–90
- [2] Simons R N 2001 *Coplanar Waveguide Circuits, Components, and Systems* (New York: John Wiley & Sons, Inc.)
- [3] Rogers J W M and Plett C 2010 *Radio frequency integrated circuit design* (Boston: Artech House)
- [4] Kandala A, Mezzacapo A, Temme K, Takita M, Brink M, Chow J M and Gambetta J M 2017 Hardware-efficient variational quantum eigensolver for small molecules and quantum magnets *Nature* **549** 242–6
- [5] Göppl M, Fragner A, Baur M, Bianchetti R, Filipp S, Fink J M, Leek P J, Puebla G, Steffen L and Wallraff A 2008 Coplanar waveguide resonators for circuit quantum electrodynamics *J. Appl. Phys.* **104** 113904
- [6] Marzouk J, Arscott S, Fellahi A E, Haddadi K, Lasri T, Christophe Boyaval and Dambrine G 2015 MEMS probes for on-wafer RF microwave characterization of future microelectronics: design, fabrication and characterization *J. Micromechanics Microengineering* **25** 075024
- [7] Mehrotra P, Chatterjee B and Sen S 2019 EM-Wave Biosensors: A Review of RF, Microwave, mm-Wave and Optical Sensing *Sensors* **19** 1013
- [8] Chen Y-F, Wu H-W, Hong Y-H and Lee H-Y 2014 40 GHz RF biosensor based on microwave coplanar waveguide transmission line for cancer cells (HepG2) dielectric characterization *Biosens. Bioelectron.* **61** 417–21
- [9] Wiemann Y, Simmendinger J, Clauss C, Bogani L, Bothner D, Koelle D, Kleiner R, Dressel M and Scheffler M 2015 Observing electron spin resonance between 0.1 and 67 GHz at temperatures between 50 mK and 300 K using broadband metallic coplanar waveguides *Appl. Phys. Lett.* **106** 193505
- [10] Mederos-Henry F, Hermans S and Huynen I 2017 Coplanar waveguide method for microwave and ferromagnetic resonance characterization of nanocarbon powders decorated with magnetic nanoparticles *Microw. Opt. Technol. Lett.* **59** 2330–5
- [11] Daffe K, Marzouk J, Fellahi A E, Xu T, Boyaval C, Eliet S, Grandidier B, Arscott S, Dambrine G and Haddadi K 2017 Nano-probing station incorporating MEMS probes for 1D device RF on-wafer characterization *2017 47th European Microwave Conference (EuMC) 2017 47th European Microwave Conference (EuMC)* (Nuremberg: IEEE) pp 831–4
- [12] Merla C, Liberti M, Marracino P, Muscat A, Azan A, Apollonio F and Mir L M 2018 A wide-band bio-chip for real-time optical detection of bioelectromagnetic interactions with cells *Sci. Rep.* **8** 5044
- [13] Gopinath A 1982 Losses in Coplanar Waveguides *IEEE Trans. Microw. Theory Tech.* **30** 1101–4

- [14] Schollhorn C, Weiwei Zhao, Morschbach M and Kasper E 2003 Attenuation mechanisms of aluminum millimeter-wave coplanar waveguides on silicon *IEEE Trans. Electron Devices* **50** 740–6
- [15] Sage J M, Bolkhovskiy V, Oliver W D, Turek B and Welander P B 2011 Study of loss in superconducting coplanar waveguide resonators *J. Appl. Phys.* **109** 063915
- [16] Woods W, Calusine G, Melville A, Sevi A, Golden E, Kim D K, Rosenberg D, Yoder J L and Oliver W D 2019 Determining Interface Dielectric Losses in Superconducting Coplanar-Waveguide Resonators *Phys. Rev. Appl.* **12** 014012
- [17] Wenner J, Barends R, Bialczak R C, Chen Y, Kelly J, Lucero E, Mariantoni M, Megrant A, O'Malley P J J, Sank D, Vainsencher A, Wang H, White T C, Yin Y, Zhao J, Cleland A N and Martinis J M 2011 Surface loss simulations of superconducting coplanar waveguide resonators *Appl. Phys. Lett.* **99** 113513
- [18] Calusine G, Melville A, Woods W, Das R, Stull C, Bolkhovskiy V, Braje D, Hover D, Kim D K, Miloshi X, Rosenberg D, Sevi A, Yoder J L, Dauler E and Oliver W D 2018 Analysis and mitigation of interface losses in trenched superconducting coplanar waveguide resonators *Appl. Phys. Lett.* **112** 062601
- [19] Wisbey D S, Gao J, Vissers M R, da Silva F C S, Kline J S, Vale L and Pappas D P 2010 Effect of metal/substrate interfaces on radio-frequency loss in superconducting coplanar waveguides *J. Appl. Phys.* **108** 093918
- [20] Quintana C M, Megrant A, Chen Z, Dunsworth A, Chiaro B, Barends R, Campbell B, Chen Y, Hoi I-C, Jeffrey E, Kelly J, Mutus J Y, O'Malley P J J, Neill C, Roushan P, Sank D, Vainsencher A, Wenner J, White T C, Cleland A N and Martinis J M 2014 Characterization and reduction of microfabrication-induced decoherence in superconducting quantum circuits *Appl. Phys. Lett.* **105** 062601
- [21] Bruno A, de Lange G, Asaad S, van der Enden K L, Langford N K and DiCarlo L 2015 Reducing intrinsic loss in superconducting resonators by surface treatment and deep etching of silicon substrates *Appl. Phys. Lett.* **106** 182601
- [22] Clarke J S, Thomas N, Roberts J, Pilliarisetty R, Yoscovits Z, Caudillo R, George H, Singh K J, Michalak D, Amin P, Mei A, Bruno A, Poletto S, Boter J, Droulers G, Kalhor N, Samkharadze N, Dehollain J P, Yeoh L, Sammak A, Scappucci G, Veldhorst M, DiCarlo L and Vandersypen L M K 2016 Quantum computing within the framework of advanced semiconductor manufacturing *2016 IEEE International Electron Devices Meeting (IEDM) 2016 IEEE International Electron Devices Meeting (IEDM)* (San Francisco, CA, USA: IEEE) p 13.1.1-13.1.3
- [23] Krantz P, Kjaergaard M, Yan F, Orlando T P, Gustavsson S and Oliver W D 2019 A quantum engineer's guide to superconducting qubits *Appl. Phys. Rev.* **6** 021318
- [24] Morello A, Tosi G, Mohiyaddin F A, Schmitt V, Mourik V, Botzem T, Laucht A, Pla J J, Tenberg S, Savvitsky R, Madzik M, Hudson F, Dzurak A S, Itoh K M, Jakob A M, Johnson B C, McCallum J C and Jamieson D N 2018 Scalable quantum computing with ion-implanted dopant atoms in silicon *2018 IEEE International Electron Devices Meeting (IEDM) 2018 IEEE International Electron Devices Meeting (IEDM)* (San Francisco, CA: IEEE) p 6.2.1-6.2.4
- [25] Shahidi G G 2002 SOI technology for the GHz era *IBM J. Res. Dev.* **46** 121–31

- [26] Lasky J B 1986 Wafer bonding for silicon-on-insulator technologies *Appl. Phys. Lett.* **48** 78–80
- [27] Kern W 1990 The Evolution of Silicon Wafer Cleaning Technology *J. Electrochem. Soc.* **137** 1887–92
- [28] Williams K R, Gupta K and Wasilik M 2003 Etch rates for micromachining processing-Part II *J. Microelectromechanical Syst.* **12** 761–78
- [29] Angermann H 2008 Passivation of structured p-type silicon interfaces: Effect of surface morphology and wet-chemical pre-treatment *Appl. Surf. Sci.* **254** 8067–74
- [30] Chabal Y J, Higashi G S, Raghavachari K and Burrows V A 1989 Infrared spectroscopy of Si(111) and Si(100) surfaces after HF treatment: Hydrogen termination and surface morphology *J. Vac. Sci. Technol. A* **7** 2104–9
- [31] Zhang X, Garfunkel E, Chabal Y J, Christman S B and Chaban E E 2001 Stability of HF-etched Si(100) surfaces in oxygen ambient *Appl. Phys. Lett.* **79** 4051–3
- [32] Raider S I 1975 Oxide Growth on Etched Silicon in Air at Room Temperature *J. Electrochem. Soc.* **122** 413
- [33] Davidson A, Jones K and Strid E 1990 LRM and LRRM Calibrations with Automatic Determination of Load Inductance *36th ARFTG Conference Digest* 36th ARFTG Conference Digest (Monterey, CA, USA: IEEE) pp 57–63
- [34] Collin R E 2001 *Foundations for microwave engineering* (New York: IEEE Press)
- [35] Bouchriha F, Grenier K, Dubuc D, Pons P, Plana R and Graffeuil J 2003 Minimization of passive circuits losses realized on low resistivity silicon using micro-machining techniques and thick polymer layers *IEEE MTT-S International Microwave Symposium Digest, 2003* IEEE MTT-S International Microwave Symposium - IMS 2003 (Philadelphia, PA, USA: IEEE) pp 959–62
- [36] Berger H H 1972 Models for contacts to planar devices *Solid-State Electron.* **15** 145–58
- [37] Ponchak G E 1999 RF Transmission Lines on Silicon Substrates *1999 29th European Microwave Conference* 1999 29th European Microwave Conference (Munich, Germany: IEEE) pp 158–61
- [38] Pfeifer T, Heiliger H–M., Stein von Kamienski E, Roskos H G and Kurz H 1995 Charge accumulation effects and microwave absorption of coplanar waveguides fabricated on high-resistivity Si with SiO₂ insulation layer *Appl. Phys. Lett.* **67** 2624–6
- [39] Wu Y, Yang S, Gamble H S, Armstrong B M, Fusco V F and Stewart J A C 1998 The effect of a SiO₂ interface layer on CPW lines and Schottky barrier diodes on HRS substrates *1998 Topical Meeting on Silicon Monolithic Integrated Circuits in RF Systems. Digest of Papers (Cat. No.98EX271)* First Topical Meeting on Silicon Monolithic Integrated Circuits in RF Systems (Ann Arbor, MI, USA: IEEE) pp 178–80
- [40] Yunhong Wu, Gamble S, Armstrong B M, Fusco V F and Stewart J A C 1999 SiO₂ interface layer effects on microwave loss of high-resistivity CPW line *IEEE Microw. Guid. Wave Lett.* **9** 10–2

- [41] Gamble H S, Armstrong B M, Mitchell S J N, Wu Y, Fusco V F and Stewart J A C 1999 Low-loss CPW lines on surface stabilized high-resistivity silicon *IEEE Microw. Guid. Wave Lett.* **9** 395–7
- [42] Reyes A C, El-Ghazaly S M, Dorn S J, Dydyk M, Schroder D K and Patterson H 1995 Coplanar waveguides and microwave inductors on silicon substrates *IEEE Trans. Microw. Theory Tech.* **43** 2016–22
- [43] Lederer D and Raskin J-P 2003 Substrate loss mechanisms for microstrip and CPW transmission lines on lossy silicon wafers *Solid-State Electron.* **47** 1927–36
- [44] Yuhang Z, Jiarong T, Xuan Z and Yong W 2009 A low-loss V-groove coplanar waveguide on an SOI substrate *J. Semicond.* **30** 074004
- [45] Neve C R, Lederer D, Pailloncy G, Kerr D C, Gering J M, McKay T G, Carroll M S and Raskin J-P 2008 Impact of Si substrate resistivity on the non-linear behaviour of RF CPW transmission lines *2008 European Microwave Integrated Circuit Conference 2008 European Microwave Integrated Circuit Conference (EuMIC) (Amsterdam, Netherlands: IEEE)* pp 36–9
- [46] Zhang Z and Yates J T 2012 Band Bending in Semiconductors: Chemical and Physical Consequences at Surfaces and Interfaces *Chem. Rev.* **112** 5520–51
- [47] Deal B E 1974 The Current Understanding of Charges in the Thermally Oxidized Silicon Structure *J. Electrochem. Soc.* **121** 198C
- [48] Deal B E 1980 Standardized Terminology for Oxide Charges Associated with Thermally Oxidized Silicon *J. Electrochem. Soc.* **127** 979
- [49] Deal B E, Sklar M, Grove A S and Snow E H 1967 Characteristics of the Surface-State Charge (Q_{ss}) of Thermally Oxidized Silicon *J. Electrochem. Soc.* **114** 266
- [50] Ang S S, Shi Y J and Brown W D 1993 Electrical characterization of low-pressure chemical-vapor-deposited silicon dioxide metal-oxide-silicon structures *J. Appl. Phys.* **73** 2397–401
- [51] Buchanan D A, Stathis J H and Wagner P R 1990 Trapped positive charge in plasma-enhanced chemical vapor deposited silicon dioxide films *Appl. Phys. Lett.* **56** 1037–9
- [52] Gaid A K and Kasprzak L A 1979 Determination of distributed fixed charge in CVD-oxide and its virtual elimination by use of HCl *Solid-State Electron.* **22** 303–9
- [53] Lee J, Chen I-C and Hu C 1986 Comparison between CVD and thermal oxide dielectric integrity *IEEE Electron Device Lett.* **7** 506–9
- [54] Sun S C and Plummer J D 1980 Electron Mobility in Inversion and Accumulation Layers on Thermally Oxidized Silicon Surfaces *IEEE J. Solid-State Circuits* **15** 562–73
- [55] Ubara H, Imura T and Hiraki A 1984 Formation of Si-H bonds on the surface of microcrystalline silicon covered with SiO_x by HF treatment *Solid State Commun.* **50** 673–5
- [56] Grant N E and Murphy J D 2017 Temporary Surface Passivation for Characterisation of Bulk Defects in Silicon: A Review *Phys. Status Solidi RRL - Rapid Res. Lett.* **11** 1700243

- [57] Kluth G J and Maboudian R 1996 Oxidation mechanism of the ammonium-fluoride-treated Si(100) surface *J. Appl. Phys.* **80** 5408–14
- [58] Weinberger B R, Deckman H W, Yablonovitch E, Gmitter T, Kobasz W and Garoff S 1985 The passivation of electrically active sites on the surface of crystalline silicon by fluorination *J. Vac. Sci. Technol. Vac. Surf. Films* **3** 887–91
- [59] Yablonovitch E, Allara D L, Chang C C, Gmitter T and Bright T B 1986 Unusually Low Surface-Recombination Velocity on Silicon and Germanium Surfaces *Phys. Rev. Lett.* **57** 249–52
- [60] Angermann H 2002 Characterization of wet-chemically treated silicon interfaces by surface photovoltage measurements *Anal. Bioanal. Chem.* **374** 676–80
- [61] Huang L J and Lau W M 1992 Effects of HF cleaning and subsequent heating on the electrical properties of silicon (100) surfaces *Appl. Phys. Lett.* **60** 1108–10
- [62] Huang L J and Lau W M 1992 Surface electrical properties of HF-treated Si(100) *J. Vac. Sci. Technol. Vac. Surf. Films* **10** 812–6
- [63] Schlaf R, Hinogami R, Fujitani M, Yae S and Nakato Y 1999 Fermi level pinning on HF etched silicon surfaces investigated by photoelectron spectroscopy *J. Vac. Sci. Technol. Vac. Surf. Films* **17** 164–9
- [64] Watanabe D, En A, Nakamura S, Suhara M and Okumura T 2003 Anomalously large band-bending for HF-treated p-Si surfaces *Appl. Surf. Sci.* **216** 24–9
- [65] Peng W, Zamiri M, Scott S A, Cavallo F, Endres J J, Knezevic I, Eriksson M A and Lagally M G 2018 Electronic Transport in Hydrogen-Terminated Si(001) Nanomembranes *Phys. Rev. Appl.* **9** 024037
- [66] Morita M, Ohmi T, Hasegawa E, Kawakami M and Ohwada M 1990 Growth of native oxide on a silicon surface *J. Appl. Phys.* **68** 1272–81
- [67] Gräf D, Grundner M, Schulz R and Mühlhoff L 1990 Oxidation of HF-treated Si wafer surfaces in air *J. Appl. Phys.* **68** 5155–61
- [68] Philipp H R and Taft E A 1982 An optical characterization of native oxides and thin thermal oxides on silicon *J. Appl. Phys.* **53** 5224–9
- [69] Renaud G, Fuoss P H, Ourmazd A, Bevk J, Freer B S and Hahn P O 1991 Native oxidation of the Si(001) surface: Evidence for an interfacial phase *Appl. Phys. Lett.* **58** 1044–6
- [70] Shimizu H and Munakata C 1990 Effects of chemical surface treatments on the generation of AC surface photovoltages in p-type silicon wafers *Semicond. Sci. Technol.* **5** 842–6
- [71] Angermann H, Dittrich Th and Flietner H 1994 Investigation of native-oxide growth on HF-treated Si(111) surfaces by measuring the surface-state distribution *Appl. Phys. Solids Surf.* **59** 193–7
- [72] Mizsei J 1991 Surface potential transients of ultrathin SiO₂/Si structures *Solid-State Electron.* **34** 951–7

- [73] Mizsei J 2002 Fermi-level pinning and passivation on the oxide-covered and bare silicon surfaces and interfaces *Vacuum* **67** 59–67
- [74] Smith R A 1978 *Semiconductors* (Cambridge: Cambridge Univ. Press)
- [75] Sameshima T, Hayasaka H and Haba T 2009 Analysis of Microwave Absorption Caused by Free Carriers in Silicon *Jpn. J. Appl. Phys.* **48** 021204
- [76] Engstrom H 1980 Infrared reflectivity and transmissivity of boron-implanted, laser-annealed silicon *J. Appl. Phys.* **51** 5245
- [77] Munakata C, Nishimatsu S, Honma N and Yagi K 1984 Ac Surface Photovoltages in Strongly-Inverted Oxidized p-Type Silicon Wafers * *Jpn. J. Appl. Phys.* **23** 1451–61
- [78] Bhadauria A, Nasimuddin, Verma A K, Sharma E K and Singh B R 2003 Optically controlled microstrip load and stub on silicon substrate *Microw. Opt. Technol. Lett.* **39** 271–6
- [79] Lee S, Kuga Y and Mullen R A 2003 Experimental results for a CW-mode optically controlled microwave switch on a silicon-based coplanar waveguide *Microw. Opt. Technol. Lett.* **36** 257–62
- [80] Barends R, Vercruyssen N, Endo A, de Visser P J, Zijlstra T, Klapwijk T M, Diener P, Yates S J C and Baselmans J J A 2010 Minimal resonator loss for circuit quantum electrodynamics *Appl. Phys. Lett.* **97** 023508
- [81] Koch J, Yu T M, Gambetta J, Houck A A, Schuster D I, Majer J, Blais A, Devoret M H, Girvin S M and Schoelkopf R J 2007 Charge-insensitive qubit design derived from the Cooper pair box *Phys. Rev. A* **76** 042319
- [82] Gao J, Daal M, Vayonakis A, Kumar S, Zmuidzinas J, Sadoulet B, Mazin B A, Day P K and Leduc H G 2008 Experimental evidence for a surface distribution of two-level systems in superconducting lithographed microwave resonators *Appl. Phys. Lett.* **92** 152505
- [83] Murray C E, Gambetta J M, McClure D T and Steffen M 2018 Analytical Determination of Participation in Superconducting Coplanar Architectures *IEEE Trans. Microw. Theory Tech.* **66** 3724–33
- [84] Lee H-J and Choi H H 2019 Microwave transmission properties of D-(+)-glucose solution with concentration variations *J. Phys. D* **52** 385401